

UC San Diego

UC San Diego Previously Published Works

Title

Large geomagnetic field anomalies revealed in Bronze to Iron Age archeomagnetic data from Tel Megiddo and Tel Hazor, Israel

Permalink

<https://escholarship.org/uc/item/6qq4n62v>

Authors

Shaar, Ron
Tauxe, Lisa
Ron, Hagai
et al.

Publication Date

2016-05-01

DOI

10.1016/j.epsl.2016.02.038

Peer reviewed



Contents lists available at ScienceDirect

Earth and Planetary Science Letters

www.elsevier.com/locate/epsl



Large geomagnetic field anomalies revealed in Bronze to Iron Age archeomagnetic data from Tel Megiddo and Tel Hazor, Israel

Ron Shaar^{a,b,*}, Lisa Tauxe^b, Hagai Ron^a, Amotz Agnon^a, Yael Ebert^a, Sharon Zuckerman^c, Israel Finkelstein^d^a The Institute of Earth Sciences, The Hebrew University of Jerusalem, Jerusalem 91904, Israel^b Scripps Institution of Oceanography, University of California San Diego, La Jolla, CA 92093-0220, USA^c The Institute of Archaeology, The Hebrew University of Jerusalem Jerusalem 91905, Israel^d The Department of Archaeology and Ancient Near Eastern Civilizations, Tel Aviv University, Tel Aviv 6997801, Israel

ARTICLE INFO

Article history:

Received 13 October 2015

Received in revised form 2 February 2016

Accepted 17 February 2016

Available online xxxx

Editor: B. Buffett

Keywords:

paleointensity

archaeomagnetism

geomagnetic anomaly

geomagnetic spikes

geomagnetic secular variations

ABSTRACT

Geomagnetic field measurements from the past few centuries show heightened secular variation activity in the southern hemisphere associated with the south Atlantic anomaly (SAA). It is uncertain whether geomagnetic anomalies at a similar scale have existed in the past owing to limited coverage and uncertainties in the paleomagnetic database. Here we provide new evidence from archaeological sources in the Levant suggesting a large positive northern hemisphere anomaly, similar in magnitude to the SAA during the 9th–8th centuries BCE, called “Levantine Iron Age anomaly”. We also report an additional geomagnetic spike in the 8th century. The new dataset comprises 73 high precision paleointensity estimates from ca. 3000 BCE to 732 BCE, and five directional measurements between the 14th and the 9th centuries BCE. Well-dated pottery and cooking ovens were collected from twenty archaeological strata in two large contemporaneous stratigraphical mounds (tells) in Israel: Tel Megiddo and Tel Hazor. The new data are combined with previously published data and interpreted automatically using the PmagPy Thellier GUI program. The Tel Megiddo and Tel Hazor data sets demonstrate excellent internal consistency and remarkable agreement with published data from Mesopotamia (Syria). The data illustrate the evolution of an extreme geomagnetic high that culminated in at least two spikes between the 11th and the 8th centuries BCE (Iron Age in the Levant). The paleomagnetic directional data of the 9th century BCE show positive inclination anomalies, and deviations of up to 22° from the averaged geocentric axial dipole (GAD) direction. From comparison of the Levantine archeomagnetic data with IGRF model for 2015 we infer the “Levantine Iron Age anomaly” between the 10th and the 8th centuries BCE is a local positive anomaly. The eastward extent of the anomaly is currently unknown.

© 2016 Elsevier B.V. All rights reserved.

1. Introduction

The geomagnetic field has changed constantly throughout Earth's history, from large-scale global events such as reversals and excursions to short temporal and spatial scale changes known as secular variation (SV). SV is among the least well constrained of the geomagnetic phenomena. Yet, it is of key interest for a number of research fields: In geophysical research SV is used to study geodynamo processes, outer core properties, and lower mantle heterogeneities (Jackson et al., 2000; Jackson and Finlay, 2007; Korte and Holme, 2010); in climatic and environmental research

SV is used to decipher the role that geomagnetism may play in controlling climate (Gallet et al., 2005, 2006; Courtillot et al., 2007; Wanner et al., 2008; Knudsen and Riisager, 2009; Ertepinar et al., 2012); in geochronology, SV helps constrain chronologies for archaeological dating (Ben-Yosef et al., 2008b; Lodge and Holme, 2009; Ben-Yosef et al., 2010; Pavon-Carrasco et al., 2011).

Recent SV data from the first two millennia BCE from Euro-Asian archaeological sources have revealed intriguing anomalies. Ben-Yosef et al. (2009) and Shaar et al. (2011) reported high field intensity fluctuations in the southern Levant (Israel and Jordan) during the 10th and the 9th century BCE that they referred to as “geomagnetic spikes”. The “spikes” are the extreme climax of a high field maximum (>160 ZAm²) in the Levant that appears in close approximation to other unusually high paleointensity values seen in Turkey (Ertepinar et al., 2012) and Georgia (Shaar et

* Corresponding author at: The Institute of Earth Sciences, The Hebrew University of Jerusalem, Jerusalem 91904, Israel. Tel.: +972 2 6584248.

E-mail address: ron.shaar@mail.huji.ac.il (R. Shaar).

<http://dx.doi.org/10.1016/j.epsl.2016.02.038>

0012-821X/© 2016 Elsevier B.V. All rights reserved.

al., 2013), and to other local maxima with lower values seen, for example, in France (Herve et al., 2013), and SE Asia (Hong et al., 2013). Thus, at least at a continental scale, the high-field episode is likely associated with a complicated field structure (Genevey et al., 2008; Kovacheva et al., 2009; Korte and Constable, 2011; Tema and Kondopoulou, 2011; Tema et al., 2012; Kovacheva et al., 2014), suggesting a complex global deviation from a simple dipole configuration (de Groot et al., 2013, 2015) that calls for further investigation.

After establishing the observation of a high field maximum in the Levant during the 10th to 9th centuries, it is now paramount to investigate its evolution through time. Also, it is of particular interest to investigate whether the Levant high field episode is a local anomaly (e.g. de Groot et al., 2015) or a global dipole feature (e.g. Hong et al., 2013). Addressing these issues is the main target of this research.

To accomplish the abovementioned objectives we investigate two key archaeological mounds (tells) in Israel: Tel Megiddo (also known as Armageddon of Revelations) and Tel Hazor. These two contemporaneous sites were of the most important settlements during the Bronze and Iron Age in the Levant, well known in biblical, Egyptian, and Mesopotamian texts. Owing to intense archaeological explorations of the sites over the past decades their chronologies are precisely dated, and hence, the sites provide invaluable well-dated archaeological material for high-resolution archaeomagnetic investigation.

The rationale for this work is as follows. First, we explore and test the robustness of our absolute paleointensity methodology by: a) deploying a recently published automatic interpretation technique (Shaar an Tauxe, 2013; Shaar et al., 2015), and b) cross-checking the two independent contemporaneous archaeomagnetic datasets. Second, we aim to deliver a comprehensive, and the most complete to date, description of paleointensity variations during the Bronze and Iron Age in the Levant by combining the overall published data. Finally, we compare the anomalies observed in the archaeomagnetic data with today's IGRF field in order to seek similar patterns between the SAA and the local Levantine high.

2. Methods

2.1. Archaeological sites

Both sites of this study hosted central cities during the Bronze and Iron Age, and were two of the most important Bronze and Iron Age settlements in the Levant. The sites controlled the international traffic route leading from Egypt to Mesopotamia and Anatolia, and witnessed the development of urbanization, religion, and technology. Both sites were continuously settled through major parts of the Bronze Age and the Iron Age until their destruction in 732 BCE in the military campaign of Tiglath Pileser III, the Assyrian ruler.

1. Tel Megiddo

Tel Megiddo (32.585N, 35.184E, Fig. 1; Armageddon of Revelations) was excavated in the beginning of the 20th century by a German team and again by the Oriental Institute of the University of Chicago. In the 1960s the Late Yigael Yadin from the Hebrew University of Jerusalem conducted further excavations. Since 1994 an extensive excavation campaign has been carried out at the site by Israel Finkelstein and David Ussishkin from Tel Aviv University, Israel.

The site was inhabited almost continuously, with no substantial occupational gaps, and succeeding settlements were built one top of the other, creating a typical multi-layered mound (tell). The absolute chronology of Tel Megiddo is well established by ceramic typology, dozens of radiocarbon samples, and historical

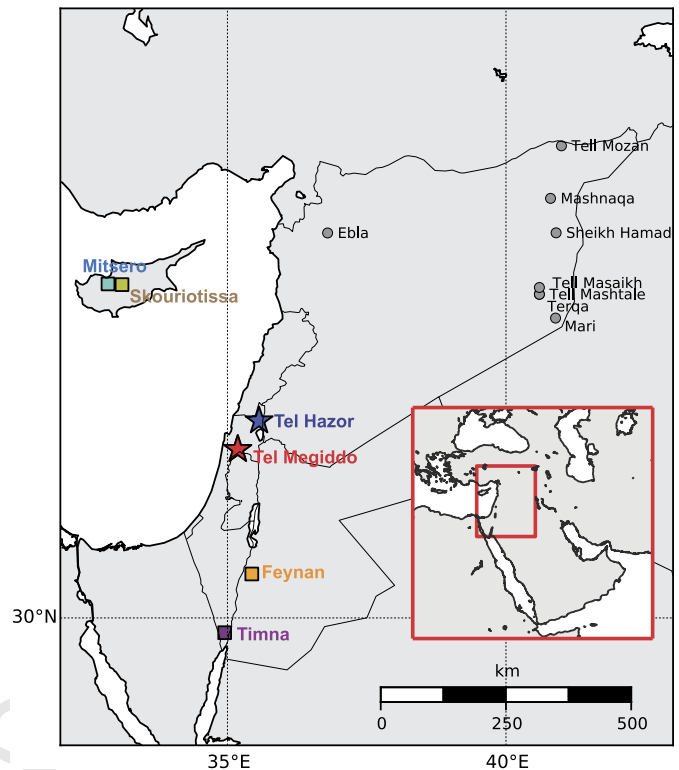


Fig. 1. Location map. Tel-Megiddo and Tel-Hazor (this study) are marked with stars. Sites with measurement data uploaded to the MagIC database (colored symbols in Fig. 5) are shown in colored squares. Other sites from Syria are shown in gray circles (open squares in Fig. 5). (For interpretation of the references to color in this figure legend, the reader is referred to the web version of this article.)

records (Finkelstein and Piasezky, 2010; Regev et al., 2014; Toffolo et al., 2014). Most significant are several destruction layers, dated by a large number of radiocarbon ages, which make the backbone of the Megiddo chronology (Finkelstein and Piasezky, 2009; Regev et al., 2014). At least one destruction layer is also securely dated historically – the one caused by the Assyrian king Tiglath-Pileser III in 732 BCE. The Early Bronze Age settlement was exceptionally large and monumental in the beginning of the 3rd millennium BCE, but experienced a decline until ca. 2000 BCE when the city started to flourish again. The Middle Bronze to Iron Age Megiddo was an important regional center – first as a Canaanite city-state and later as an administrative center of the Northern Kingdom of Israel. It is represented by a complete sequence of occupation until its destruction in 732 BCE.

For this study we collected pottery material from ten well-dated strata in four different Areas of the Tel Aviv Expedition, labeled J, F, K, and H. In addition, we sampled five *in situ* cooking ovens (tabuns) during the 2010–2011 excavation seasons from Areas K, Q, and H. Complete information on the areas, strata, and samples (listed in the Supplementary Material) can be found in the published excavation reports (available online from megiddo.ittau.ac.il/).

2.1.2. Tel Hazor

Tel Hazor (33.017N, 35.568E, Fig. 1) was first excavated in the 1950s and 1960s under the direction of Late Yigael Yadin from the Hebrew University of Jerusalem. Excavations were re-initiated in 1990 under the direction of Amnon Ben-Tor from the Hebrew University, and continue annually to the present.

The extensive excavations revealed over 20 superimposed stages in two distinct sections: the upper city that includes an acropolis, and a lower city with a fortified enclosure. The

Early Bronze settlement of Hazor was confined to the upper city (Zuckerman, 2013b) and the settlement expanded to the lower city during the Middle Bronze Age (Zuckerman, 2013a). The Late Bronze Hazor featured an impressive massive palace in the acropolis, which was destroyed during the 13th century in an intense fire (Zuckerman, 2010). In the 11th century BCE, the settlement was rebuilt (Ben-Ami, 2013) and was settled continuously through the Iron age (Ben-Tor, 2013) until its destruction at 732 BCE by the Assyrian Tiglath-Pileser III.

For this study we collected pottery from eight strata spanning the second half of the 3rd millennium BCE to the 732 BCE destruction. Complete information on the strata and samples (listed in the Supplementary Material) can be found in Tel Hazor published excavation reports (available online from <http://hazor.huji.ac.il/>).

2.2. Sampling

From each stratum we collected at least four pottery vessels (i.e. “samples”) for paleointensity analysis. When possible, we preferred thin, fine-grained, well burnt pottery vessels from whole, or restored vessels. Preference was given to domestic cheap vessels, as it is more likely that these objects were manufactured near the site, and best fit the chronological context of the archaeological stratum from which they were found. The pottery samples were collected from storehouses located at the Institute of the Archaeology, Tel Aviv University, the Institute of Archaeology, the Hebrew University of Jerusalem, and from the Israel Antiquities Authority. An Excel file in the Supplementary Material lists the excavation details of the samples (Locus, Basket, Date, and additional archaeological information). A total of 111 pottery samples were analyzed: 66 from Tel Megiddo, and 45 from Tel Hazor.

In addition to the pottery collections (which are by nature unoriented), we sampled five in situ cooking ovens (tabuns) for full-vector paleomagnetic analyses. These are round installations made of clay, each about 1 m in diameter. Two ovens (mgq04t1 and mgq05t1) were sampled by carving horizontally leveled cubes on the oven’s wall, and gluing them inside standard paleomagnetic sampling cubes. The other three were sampled by marking azimuth and inclination in as many locations as possible on the oven’s surface using a Brunton compass, and carefully removing the oriented pieces. Each oriented piece was cut into one or two smaller cube-shaped specimens. The specimens were glued inside standard plastic paleomagnetic sampling cubes keeping the information of field orientation. The exposure of three ovens (c6-q4, 5-q5, H12) allowed sampling from the entire periphery of the round-shaped oven. The other two ovens (G5-q5, K9) comprised of only a sector of the installation.

2.3. Paleointensity

2.3.1. Laboratory procedures

From each potsherd (“sample”) we subsampled 4–10 smaller fragments (“specimens”). Each specimen was wrapped in fiberglass filter paper and glued inside a glass vial, 12 mm in diameter, using Potassium Silicate (KASIL) glue. Paleointensity experiments were carried out at the paleomagnetic laboratory of Scripps Institution of Oceanography (SIO), University of California San Diego, using laboratory built paleointensity ovens, and at the paleomagnetic laboratory of the Institute of Earth Sciences, the Hebrew University of Jerusalem (HUJI), using a modified ASC TD-48 oven (Shaar et al., 2010). The experimental procedure followed the IZZI protocol of Tauxe and Staudigel (2004) with routine pTRM checks at every second temperature step (Coe et al., 1978). Different batches used different values of oven field: 40 μ T, 60 μ T, 70 μ T, and 80 μ T, to detect and, if necessary, compensate for non-linearity of TRM acquisition, if detected.

Anisotropy of thermoremanent magnetization (ATRM) tensors were calculated for all paleointensity specimens. The ATRM procedure consists of eight heating steps carried out at the highest temperature that the specimens reached during the Thellier experiment: a baseline step in a zero field (subtracted from the subsequent in-field measurements), six in-field steps at orthogonal directions (+x, +y, +z, -x, -y, -z), and an additional in-field alteration check at the end of the experiment. As the high temperature procedures can cause alteration, we calculated an alteration statistic from the vector differences of four pairs of measurements: $(-x, +x)$, $(-y, +y)$, $(-z, +z)$, and (first measurement with alteration-check measurement). If the difference exceeded 5% for any one of these pairs, we rejected the ATRM results, and measured the anisotropy of anhysteretic remanent magnetization (AARM). AARM was determined in 9 of the 15 position measurement scheme of Jelinek (1978) (see also Tauxe, 2010) using 180 mT AC field and 100 μ T DC field. Before each ARM step, the specimen was AF demagnetized at 180 mT and this baseline magnetization was subtracted from the subsequent in-field ARM measurements. Anisotropy tensors were calculated using the method of Hext (1963) (see also Tauxe, 2010) via PmagPy software (<http://earthref.org/PmagPy/cookbook>) using the Thellier GUI program (Shaar and Tauxe, 2013) incorporated into the Pmag GUI (formerly QuickMagC.py) program.

The effect of cooling rate was measured on all paleointensity specimens, unless severe alteration occurred during the preceding measurements. The procedure is similar to that described in Chauvin et al. (2000) and Genevey and Gallet (2002), and consists of four steps cooling from 590 °C: a baseline zero-field step, an in-field step in a fast (regular) cooling rate, an in-field step in a slow cooling rate, and finally, an in-field alteration check step in a fast cooling rate. A cooling rate correction was calculated assuming a logarithmic relation between TRM overestimation and the ratio between cooling rates (Halgedahl et al., 1980; Genevey and Gallet, 2002). The cooling rate correction was rejected if alteration exceeded 5%. If the cooling rate correction could not be calculated for a given specimen, we used the averaged correction factor from the sister specimens from the same potsherd sample. In our calculation we assumed an averaged ancient cooling rate of 6 h from 500 °C to 200 °C for all the archaeological samples. For more explanation see Supplementary Material Figures S1, S2.

The possibility of nonlinear TRM acquisition behavior (NLT) (Selkin et al., 2007) was checked for 31 specimens using 5 in-field steps at 570 °C: 20, 40, 50, 80, 110 μ T. The results demonstrated that the NLT effect is insignificant for the pottery material, and therefore, the rest of the specimens were not subjected to the NLT procedure.

2.3.2. Automatic data analyses

In this work we apply the PmagPy program Thellier GUI (Shaar and Tauxe, 2013) for interpretation of the paleointensity data. We adopted the automatic interpretation approach over the conventional manual interpretation technique because the large amount of data from the Levant (see section 4.1) necessitates a fast, reproducible, and objective interpretation method with robust and realistic error estimation.

In the automatic interpretation the Thellier GUI user first has to choose acceptance criteria, from the list given in Paterson et al. (2014); <http://www.paleomag.net/SPD>. Using these criteria the Thellier GUI program performs the following tasks:

1. Line fitting to the Arai plot: The program analyzes all the possible best-fit lines of each Arai plot separately and filters out the interpretations (best-fit lines) that fail the specimen acceptance criteria.

Table 1
Acceptance criteria

Criteria group	Statistic	Threshold value	Description	Reference ^b
Specimen paleointensity ^a	FRAC	0.79	Fraction parameter	[1]
	β	0.1	Scatter parameter	[2], [3]
	SCAT	True	Scatter parameter	[1]
	N_{PTRM}	2	Number of pTRM checks	
	n	4	Number of data points	
	MAD	5	Maximum Angular Deviation of the zero field steps	[4]
	DANG	10	Deviation Angle	[5]
Sample paleointensity	Alteration check (correction)	5%	Alteration check in Non-Linear-TRM, TRM anisotropy, and cooling rate measurements	
	N_{min}	3	Minimum number of specimens with anisotropy correction	
	$N_{\text{min_aniso_corr}}$	At least half of the specimens	Minimum number of specimens with anisotropy correction	
	$N_{\text{min_cr_corr}}$	1	Minimum number of specimens with cooling rate correction	
	σ	$\sigma < 3 \mu\text{T}$ OR $\sigma \% < 8\%$	Standard deviation of the sample mean	
	Anisotropy sample test	1%	If the mean anisotropy correction of all the specimens from the same sample is higher than 5% then specimens without anisotropy correction are discarded	
Specimen direction	MAD	5	Maximum Angular Deviation	[4]
Sample direction	N	8	Minimum number of specimens for mean calculation	
	κ	50	Fisher precision parameter	[6]

^a For a complete description and definitions see Paterson et al. (2014) (<http://www.paleomag.net/SPD/>).

^b [1]: Shaar and Tauxe (2013); [2]: Coe et al. (1978); [3]: Selkin and Tauxe (2002); [4]: Kirschvink (1980); [5] Tauxe and Staudigel (2004); [6] Fisher (1953).

2. Applying corrections: each interpretation that passes step #1 above is corrected for the effect of anisotropy, cooling rate, and nonlinear-TRM (NLT).
3. Sample/site mean calculation: the program calculates all the possible sample/site means permutations from the acceptable specimen interpretations and isolates all the means that pass the sample/site acceptance criteria.
4. STDEV-OPT sample/site mean calculation: from all the sample/site means that pass the criteria, the STDEV-OPT mean ("most likely") is the one that has the lowest coefficient of variation statistic [$\sigma \% = 100 * (\sigma / \text{mean})$], the best index for agreement within a cooling unit or site. This mean and its associated standard deviation is called hereafter the "STDEV-OPT mean" (i.e., "standard deviation optimization").
5. Calculating extended error bounds: uncertainty bounds are calculated by taking from all the possible means calculated in step #3 above the two end case interpretations with the lowest and the highest paleointensity, including the standard deviation error [these end case values are: $(B_{\text{min}} - \sigma)$ and $(B_{\text{max}} + \sigma)$]. The interval bounded by these values is referred to hereafter as the "extended error bounds". The extended error bound is significantly larger than what is typically used as error estimation (standard deviation of the mean). Nevertheless, this calculation is more robust as it takes into consideration all the possible interpretations at the specimen level that pass the criteria, and not just one set of "acceptable" interpretations chosen by the analyst.

2.4. Paleomagnetic directions

From each oven eight to twelve specimens were AF demagnetized in increments of 5 mT or 10 mT up to a peak field of 60, 70, 80, or 100 mT. Best-fit paleomagnetic directions were calculated using principle component analysis (Kirschvink, 1980). Paleomagnetic means were calculated using Fisher statistics (Fisher, 1953).

Data were analyzed using the Demag GUI program, a recent contribution to the open code PmagPy software (<http://earthRef.org/PmagPy/>).

2.5. Acceptance criteria

Table 1 lists the acceptance criteria we used. For paleointensity these include a set of eight statistics at the specimen level checking the fraction of remanence, scatter, linearity, and alteration effects of the Arai plots, and the linearity and the convergence to the origin of the vector end-point plots. Representative examples of specimens failing different paleointensity statistics are shown in Figs. 2b–f. At the sample level acceptance criteria include threshold values for the number of specimens needed for sample mean calculation, an upper limit for the standard deviation, and criteria for the anisotropy and cooling rate corrections. For paleomagnetic directions we used upper bounds for the MAD statistic (Kirschvink, 1980) and the precision parameter (Fisher, 1953). For a detailed explanation of paleomagnetic statistics see Paterson et al. (2014) (<http://www.paleomag.net/SPD/>).

We consider the criteria listed in Table 1 as the optimal choice for screening out unreliable data. Yet, this is a subjective user-defined choice. Therefore, if one wishes to reanalyze the data published here using different criteria or different interpretation guidelines we make it possible. All the measurement data are accessible from the MagIC database (<http://earthRef.org/MagIC/11028/>). The PmagPy programs used to analyze the data (Pmag GUI, Demag GUI, and Thellier GUI) are available from the PmagPy Cookbook page (<http://earthRef.org/PmagPy/>).

3. Results

3.1. Paleointensity

We analyzed a total of 592 specimens (388 from Megiddo and 204 from Hazor) collected from 111 pottery samples (66 from

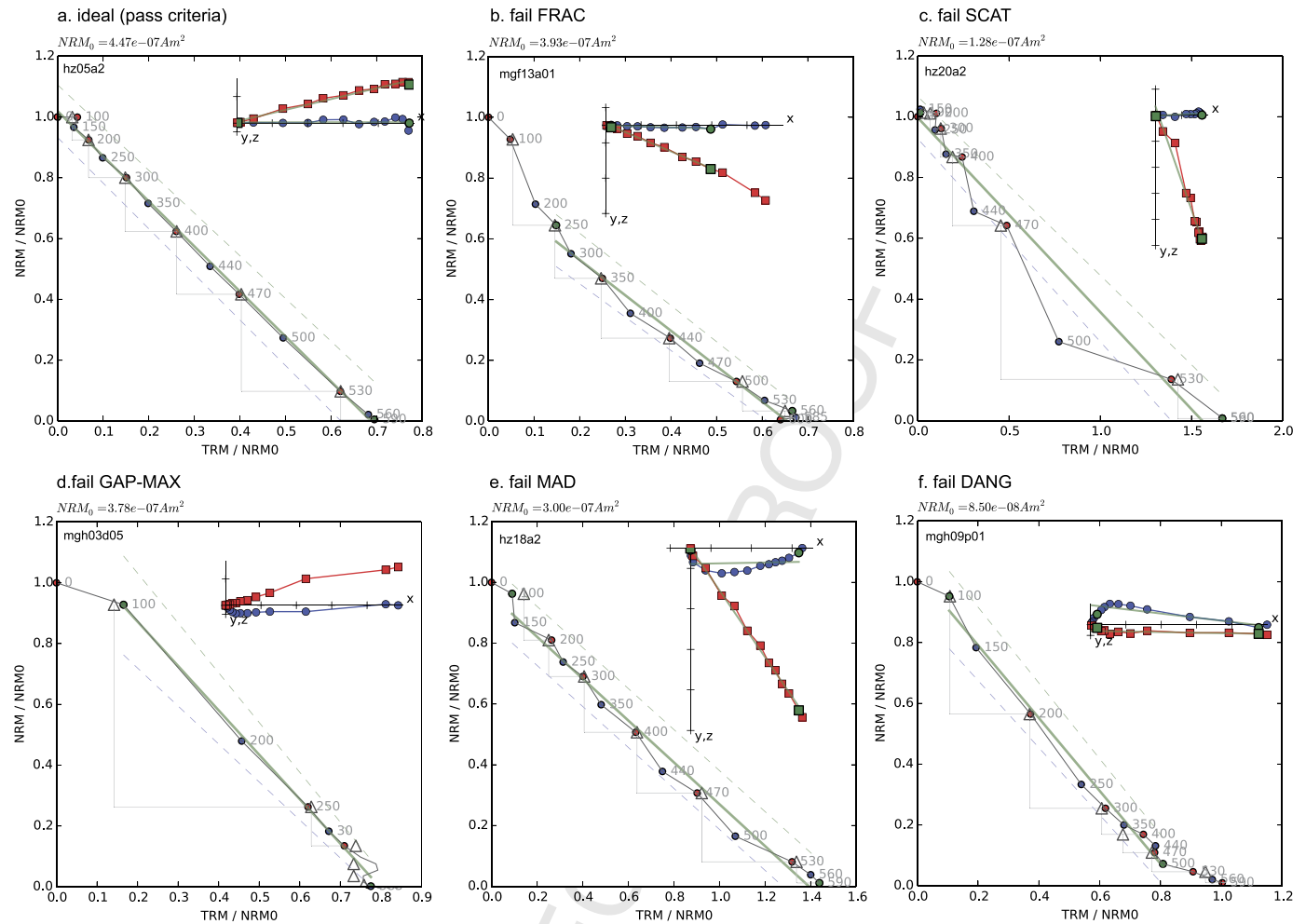


Fig. 2. Representative Arai plots showing different behaviors and interpretations. Red/blue circles and triangles are ZI, IZ steps, and pTRM checks, respectively. Blue (red) squares in the Zijdeveld plots (insets) are x - y (x - z) projections of the NRM in specimen coordinate system, where x -axis is rotated to the direction of the NRM. Best-fit lines and temperature bounds are marked in green. (a) Ideal behavior passing all criteria. (b)–(f) Interpretations passing all criteria except FRAC (b), SCAT (c), GAP-MAX (d), MAD (e), and DANG (f). See text for details. (For interpretation of the references to color in this figure legend, the reader is referred to the web version of this article.)

Megiddo and 45 from Hazor) and 5 ovens. A total of 416 specimens (success rate of 70%) and 73 samples (success rate of 66%) passed the acceptance criteria. We consider these acceptance rates high given the strict criteria we choose (Table 1). Fig. 2a shows a representative case of a specimen passing the criteria. Figs. 2b–f show examples of rejected interpretations. Fig. S3, Supplementary Material shows histograms summarizing the specimens paleointensity statistics. One significant observation is that the anisotropy correction is typically in the range of several percent, but a considerable number of specimens have much higher corrections of more than 10%. The cooling rate correction factor is typically smaller than 10%.

Sample level paleointensity data are listed in Table 2 and shown in Fig. 3, where Tel Megiddo and Tel Hazor are shown in red and blue, respectively. Solid symbols in Fig. 3 represent the STDEV-OPT means and the y -axis error bars represent the “extended error bounds” (see section 2.3.2 for explanation). Seventeen different strata with pottery samples are displayed, sixteen of which include 3 or more samples. There is an excellent agreement between the two independent datasets, supporting two of our working hypotheses: A) Consistency of the independent archaeological chronologies of Tel-Megiddo and Tel-Hazor, and B) Reliability of the paleointensity procedures and the automatic interpretation technique. The four ovens that passed the criteria agree within er-

ror with the pottery data [stratum K-09 (ca. 1350 BCE), H-12 (ca. 1125 BCE), and Q-05 (ca. 900 BCE)]. This provides another validation for the paleointensity procedures.

We note some interesting features in the data shown in Fig. 3. The field intensity before ca. 1800 BCE was 30–50 μ T, that is, of the order of today’s field (44 μ T). After a minimum at the 18th century BCE (F-13), the field gradually increased, and from the 13th century BCE onward the field reached very high values of between 50–95 μ T (Fig. 3b). The climax of this high field episode has a double peak shape: a maximum at ca. 1000 BCE (stratum H-09 in Megiddo), a minimum during the 9th century BCE (stratum H-07 in Megiddo) and a second maximum at ca. 740 BCE (just before the destruction layers H-03 in Megiddo and Hazor V/VI). The latter is characterized with a large scatter of the data at both sites and overlapping error bars suggesting that the field changed rapidly during the time interval represented by the layers.

3.2. Paleomagnetic directions

Fig. 4a shows two representative Zijdeveld plots showing straight demagnetization behavior converging to the origin. As shown, some specimens have coercivity spectra of a few tens of militesla, while others exceed 120 mT (the maximum field

Table 2
Samples paleointensity^a.

Stratum	Age (BCE)	Sample	N	$B \pm \sigma$	VADM $\pm \sigma$	B extended errorbar	VADM extended errorbar
Hazor V	740 (800–732)	hz05a	3	88.15 ± 0.27	165.8 ± 0.5	83.4–93.8	156.8–176.4
		hz05b	7	75.69 ± 4.49	142.3 ± 8.5	69.9–83.8	131.5–157.6
		hz05c	6	83.15 ± 0.34	156.4 ± 0.7	79.1–86.2	148.8–162.1
		hz05e	5	67.60 ± 0.39	127.1 ± 0.8	65.6–72.5	123.4–136.3
		hz05f	5	81.52 ± 1.90	153.3 ± 3.6	75.5–86.2	142.0–162.1
		hz05g	6	73.26 ± 1.73	137.8 ± 3.2	70.2–76.4	132.0–143.7
Hazor VI		hz06a	7	67.81 ± 3.12	127.5 ± 5.9	63.1–73.0	118.7–137.3
		hz06b	5	70.66 ± 0.76	132.9 ± 1.4	63.9–74.5	120.2–140.1
		hz06c	3	77.69 ± 0.03	146.1 ± 0.0	75.1–81.5	141.2–153.3
Hazor VII	850 (900–800)	hz07a	4	64.37 ± 0.21	121.1 ± 0.4	58.7–71.6	110.4–134.7
		hz07b	5	72.03 ± 0.50	135.5 ± 1.0	68.5–78.0	128.8–146.7
		hz07c	5	57.08 ± 3.26	107.3 ± 6.1	51.5–63.6	96.9–119.6
		hz07d	6	68.62 ± 2.80	129.1 ± 5.3	64.1–73.7	120.6–138.6
		hz07e	3	75.79 ± 1.54	142.5 ± 2.9	71.4–80.8	134.3–152.0
Hazor IX	950 (1000–900)	hz09a	4	66.24 ± 1.63	124.6 ± 3.0	62.2–70.1	117.0–131.8
Hazor X		hz10b	3	77.27 ± 0.05	145.3 ± 0.1	67.0–80.8	126.0–152.0
		hz10c	4	64.79 ± 2.90	121.8 ± 5.4	58.7–70.6	110.4–132.8
		hz10d	3	65.91 ± 1.25	124.0 ± 2.4	62.1–69.4	116.8–130.5
Hazor XI	1050 (1100–1000)	hz11a	3	68.39 ± 0.03	128.6 ± 0.0	62.8–71.1	118.1–133.7
		hz11b	3	61.14 ± 0.08	115.0 ± 0.1	57.8–67.3	108.7–126.6
		hz11c	4	59.44 ± 3.08	111.8 ± 5.8	54.9–64.3	103.2–120.9
Hazor XIII	1250 (1350–1250)	hz13a	7	60.22 ± 1.72	113.3 ± 3.2	54.7–69.0	102.9–129.8
		hz13b	5	55.12 ± 1.00	103.7 ± 1.9	52.9–62.3	99.5–117.2
		hz13e	6	59.96 ± 0.28	112.8 ± 0.5	55.0–65.3	103.4–122.8
		hz13f	3	56.66 ± 0.20	106.6 ± 0.4	55.5–61.4	104.4–115.5
Hazor XV	1550 (1650–1450)	hz15a	3	50.11 ± 0.04	94.2 ± 0.0	48.2–54.4	90.6–102.3
		hz15b	3	48.79 ± 1.57	91.8 ± 3.0	46.1–51.5	86.7–96.9
Hazor XVIII	2200 (2300–2000)	hz18a	4	45.00 ± 0.57	84.6 ± 1.1	42.0–48.0	79.0–90.3
		hz18d	4	47.83 ± 0.45	90.0 ± 0.9	45.8–51.2	86.1–96.3
		hz18e	3	46.29 ± 0.03	87.1 ± 0.0	44.4–49.8	83.5–93.7
Hazor XX	2700 (2800–2500)	hz20b	4	42.03 ± 1.17	79.0 ± 2.2	39.6–43.6	74.5–82.0
		hz20c	6	42.53 ± 0.97	80.0 ± 1.8	37.5–46.0	70.5–86.5
		hz20e	3	31.40 ± 1.08	59.1 ± 2.1	30.3–32.9	57.0–61.9
		hz20f	3	36.33 ± 0.84	68.3 ± 1.6	34.8–39.2	65.4–73.7
Megiddo F-10	1450 (1500–1400)	mgf10a	4	49.72 ± 0.59	94.0 ± 1.1	47.0–53.4	88.9–101.0
		mgf10b	5	49.99 ± 2.83	94.5 ± 5.4	46.0–54.5	87.0–103.1
		mgf10d	4	52.16 ± 2.26	98.6 ± 4.2	47.4–57.5	89.6–108.7
Megiddo F-13	1800 (1900–1700)	mgf13b	7	38.38 ± 1.77	72.6 ± 3.4	34.2–42.1	64.7–79.6
		mgf13d	6	42.66 ± 0.89	80.7 ± 1.7	40.5–46.1	76.6–87.2
		mgf13e	6	43.24 ± 2.47	81.8 ± 4.7	38.7–47.5	73.2–89.8
		mgf13f	4	42.84 ± 0.20	81.0 ± 0.4	39.3–46.9	74.3–88.7
Megiddo H-03	740 (800–732)	mgh03b	5	75.12 ± 2.64	142.1 ± 5.0	66.7–83.5	126.1–157.9
		mgh03f	5	80.46 ± 2.58	152.1 ± 4.8	71.4–89.3	135.0–168.9
		mgh03g	8	93.44 ± 4.60	176.7 ± 8.7	83.3–105.0	157.5–198.6
		mgh03h	7	75.86 ± 3.13	143.5 ± 6.0	68.6–83.8	129.7–158.5
		mgh03i	6	79.86 ± 1.20	151.0 ± 2.3	69.2–86.3	130.9–163.2
		mgh03j	3	89.74 ± 0.40	169.7 ± 0.8	80.4–91.8	152.0–173.6
Megiddo H-07	900 (950–850)	mgh07b	3	74.66 ± 2.53	141.2 ± 4.8	70.4–82.3	133.1–155.6
		mgh07d	5	67.81 ± 2.41	128.2 ± 4.6	59.2–77.4	111.9–146.4
Megiddo H-09	1000 (1050–950)	mgh09h	5	66.44 ± 0.31	125.6 ± 0.6	65.4–69.8	123.7–132.0
		mgh09j	4	73.71 ± 0.03	139.4 ± 0.0	71.7–76.2	135.6–144.1
		mgh09k	5	82.93 ± 0.06	156.8 ± 0.1	70.8–85.9	133.9–162.4
		mgh09l	4	83.58 ± 0.46	158.0 ± 0.9	75.4–89.5	142.6–169.2
		mgh09m	6	67.13 ± 2.71	126.9 ± 5.1	61.2–70.6	115.7–133.5
Megiddo H-12	1125 (1150–1100)	mgh12t1PI	3	60.73 ± 0.64	114.8 ± 1.2	55.3–65.6	104.6–124.0
Megiddo J-04	3000 (3100–2900)	mgj04a	4	30.92 ± 1.48	58.5 ± 2.8	28.6–33.4	54.1–63.2
		mgj04b	4	41.56 ± 2.32	78.6 ± 4.4	37.5–45.7	70.9–86.4
		mgj04d	8	35.30 ± 2.30	66.8 ± 4.3	31.7–39.0	59.9–73.7
Megiddo J-06	2700 (2600–2800)	mgj06a	4	38.42 ± 2.98	72.7 ± 5.6	35.4–41.7	66.9–78.9
		mgj06b	3	40.06 ± 0.41	75.8 ± 0.8	34.7–42.2	65.6–79.8
		mgj06c	4	40.25 ± 1.27	76.1 ± 2.4	37.9–46.4	71.7–87.7
		mgj06d	4	38.27 ± 0.78	72.4 ± 1.4	34.9–41.2	66.0–77.9

(continued on next page)

Table 2 (continued)

Stratum	Age (BCE)	Sample	N	$B \pm \sigma$	VADM $\pm \sigma$	B extended errorbar	VADM extended errorbar
Megiddo K-06	1130 (1130–1180)	mgk06a	5	66.60 ± 0.83	125.9 ± 1.5	63.2–75.3	119.5–142.4
		mgk06b	3	62.36 ± 3.03	117.9 ± 5.8	56.2–69.1	106.3–130.7
		mgk06c	4	62.37 ± 2.45	117.9 ± 4.6	56.6–66.6	107.0–125.9
		mgk06d	5	60.69 ± 0.46	114.8 ± 0.8	55.1–64.4	104.2–121.8
Megiddo K-08	1250 (1300–1200)	mgk08a	3	58.77 ± 0.77	111.1 ± 1.4	56.8–63.5	107.4–120.1
		mgk08b	4	59.07 ± 3.43	111.7 ± 6.5	54.0–66.0	102.1–124.8
		mgk08c	4	62.92 ± 0.25	119.0 ± 0.5	56.7–67.7	107.2–128.0
		mgk08e	5	55.62 ± 0.83	105.2 ± 1.6	51.0–60.5	96.4–114.4
Megiddo K-09	1350 (1400–1300)	mgk09t1PI	3	52.38 ± 3.99	99.1 ± 7.5	48.1–56.4	91.0–106.7
Megiddo Q-05	900 (950–850)	mgq05t1PI	3	68.67 ± 0.69	129.9 ± 1.3	62.4–81.2	118.0–153.5
		mgq05t2PI	6	64.17 ± 1.25	121.3 ± 2.4	61.4–72.6	116.1–137.3

^a σ is the standard deviation of the STDEV-OPT mean, and the extended error bar is the error envelope calculated by the Thellier GUI (shown in Figs. 3, 5). See section 2.3.2 for details.

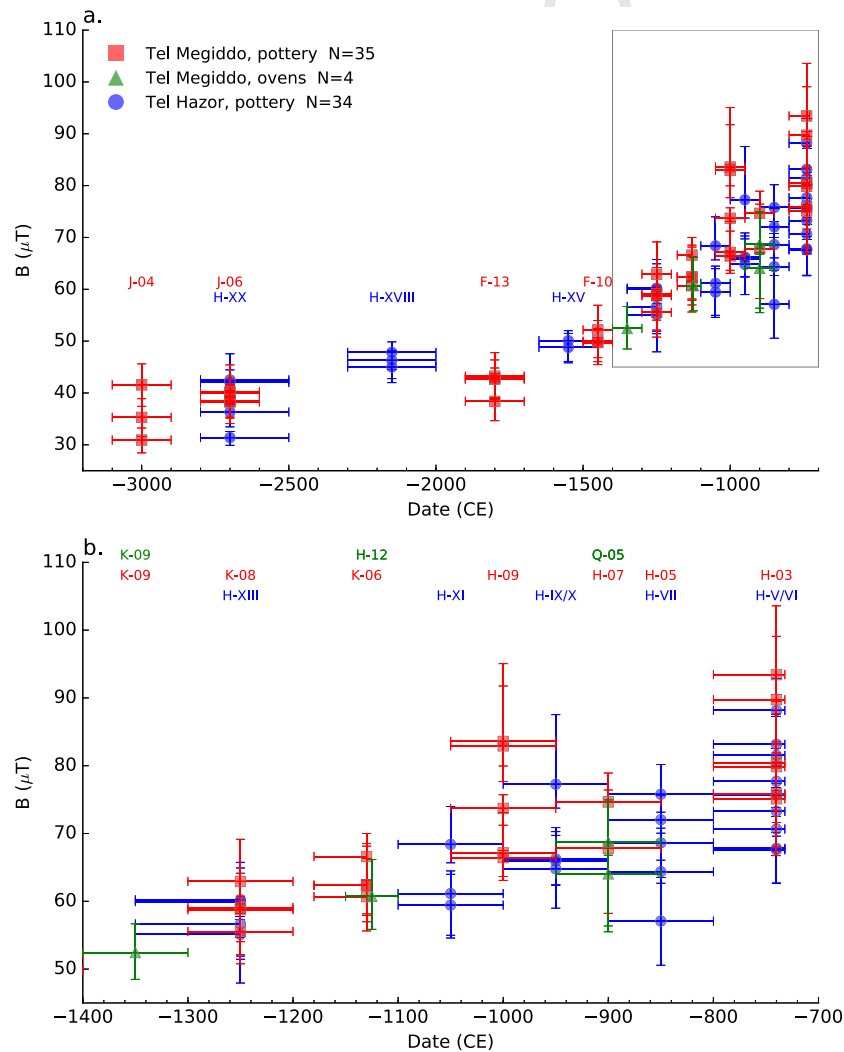


Fig. 3. New paleointensity results from ca. 3000 BCE to ca. 732 BCE. There is excellent agreement between two independent datasets of Tel Megiddo (red, green) and Tel Hazor (blue). (b) is a magnification marked as rectangle in (a), showing the evolution of the Iron Age Levantine Anomaly with the double-peak maximum at ca. 1000 BCE and ca. 740 BCE. (For interpretation of the references to color in this figure legend, the reader is referred to the web version of this article.)

currently available in the HUJI lab). Fig. 4b shows equal area projections of the five ovens (i.e. sites). Paleomagnetic statistics are given in Table 3. All sites have a precision parameter k (Fisher, 1953) larger than 50. Four ovens have $k > 130$ and $\alpha_{95} < 4$, while oven mgq04t1 have marginal statistics ($k = 54$ and $\alpha_{95} = 6.2$).

A considerable angular deviation from the averaged GAD (geocentric axial dipole) inclination in Megiddo (52.0 , Table 3) is observed in the two ovens collected from stratum Q-5 (ca. 900 BCE). This deviation of 17° – 23° is associated with a period when the field strength was very high (Fig. 4). This consequential result is further discussed in the following.

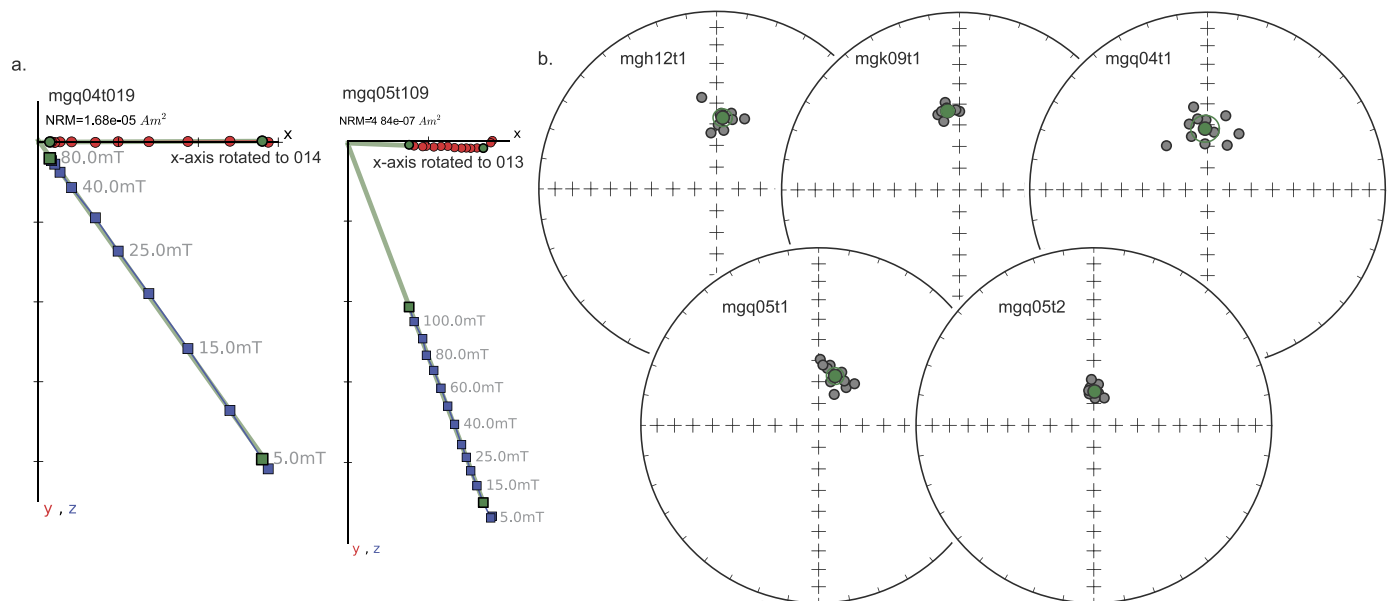


Fig. 4. Demagnetization experiments on five ovens from Megiddo. (a) Representative Zijderveld plots showing straight demagnetization curves. (b) Equal area projections showing specimens best-fit directions (gray) and Fisher means (green). (For interpretation of the references to color in this figure legend, the reader is referred to the web version of this article.)

Table 3
Tel-Megiddo ovens paleomagnetic mean directions.

Oven	Stratum	Age (BCE)	Declination	Inclination	N	k	α_{95}	Deviation from GAD ^a
mgk09t1	Megiddo K-09	1350 (1400–1300)	351.5	53.0	8	395	2.8	5.3
mgh12t1	Megiddo H-12	1125 (1150–1100)	4.8	56.9	10	131	4.2	5.7
mgq05t1	Megiddo Q-05	900 (950–850)	18.4	66.1	11	140	3.9	16.9
mgq05t2	Megiddo Q-05	900 (950–850)	1.3	74.5	11	565	1.9	22.5
mgq04t1	Megiddo Q-04	850 (900–800)	357.7	61.8	11	54	6.3	9.9

^a The averaged GAD inclination in Megiddo is 52.0

4. Discussion

4.1. Levant paleointensity compilation

The Levant region, including Israel, Egypt, Jordan, Cyprus, Syria, and Southern Turkey has been subject to a number of archaeointensity studies over the past decades (see list of 24 references in the Supplementary material). These published data are available online from the GEOMAGIA database (Korhonen et al., 2008; Brown et al., 2015) and from published data compilations such as Genevey et al. (2008). Fig. S4, Supplementary Material, displays all the Levantine paleointensity data published to date. The resulting picture is complicated, noisy, and shows some significant internal discrepancies. This is not surprising as these different datasets were obtained using different experimental methods, laboratory protocols, interpretation and error estimation approaches, selection criteria, averaging schemes, and assessment of anisotropy and cooling rate corrections. In addition, some legacy data employ different and sometime contradicting and irreproducible dating methodologies, and in cases, outdated chronologies.

Settling all data discrepancies shown in Fig. S4 is beyond the scope of the present study. Instead, we wish to provide the most consistent regional dataset that can be used in interrelated studies, such as archaeomagnetic dating and geodynamo research. To achieve this aim we seek to minimize as many sources of uncertainty as possible. We argue that the optimal approach to minimize paleointensity uncertainties is the automatic interpretation technique used here and in Shaar et al. (2015) (see Section 2.3.2 for details). The rationale for this approach is supported by the internal consistency shown in Fig. 3. The automatic interpretation

technique can be applied only on studies that published the entire measurement data (Ben-Yosef et al., 2008a, 2008b; Ben-Yosef et al., 2009; Shaar et al., 2011; Shaar et al., 2015). We therefore have downloaded these data from the MagIC database and re-interpreted them (along with those of the current study) using the criteria given in Table 1 to guarantee a consistent interpretation. We also apply a dating criterion following the “Age Quality” index of Ben-Yosef et al. (2008a, 2008b), whereby only “grade 1” (“Excellent”) are included. The combined measurement data file consists of 97,219 measurement lines, 2331 specimens, and 532 samples. This large dataset is expected to grow with future studies but is easily interpreted using the automatic interpretation technique incorporated in Thellier GUI.

Fig. 5 displays the Levant MagIC-based interpretations, converted to Virtual Axial Dipole Moments (VADM, see Tauxe et al., 2005) in colored symbols, where the symbols and the error bars show the STDEV-OPT means and the “extended” error bounds (see Section 2.3.2 for details). The data used to generate Fig. 5 are provided in the Supplementary Material. We note, that some samples previously reported in results tables of published articles do not pass the stricter criteria we used here, and therefore do not appear in Fig. 5 (also Supplementary Material). Legacy data that do pass our new criteria show very similar values to the already published results, however. We also plot in open black symbols other data from Syria published by two research groups: IGP, Paris (e.g. Genevey et al., 2003; Gallet et al., 2005, 2006, 2008, 2014, 2015; Gallet and Butterlin, 2015), and the Institute for Rock Magnetism (IRM), University of Minnesota (Stillinger et al., 2015). These Syrian data were published without the measurement data and cannot be re-interpreted via Thellier GUI using our criteria. The main reasons for

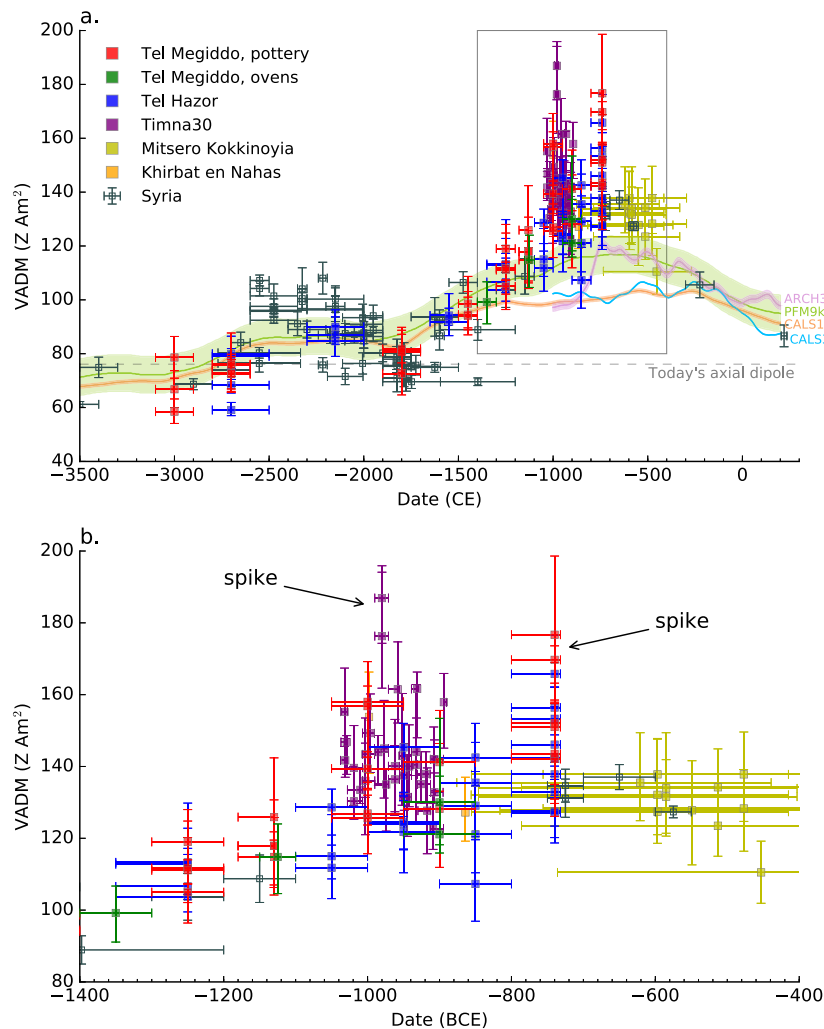


Fig. 5. Geomagnetic field intensity in the Levant from 3500 BCE to 400 BCE. Colored filled symbols show sites with measurement data in the MagIC database (Ben-Yosef et al., 2008a, 2008b, 2009; Shaar et al., 2011, 2015), interpreted using the automatic interpretation technique described in text and the acceptance criteria listed in Table 1. Open gray symbols are other published data from Syria (Genevey et al., 2003; Gallet et al., 2005, 2006, 2008, 2014, 2015; Gallet and Le Goff, 2007; Gallet and Butterlin, 2015; Stillinger et al., 2015). Locations map is shown in Fig. 1. Solid curves show prediction of global geomagnetic models (Korte et al., 2009, 2011; Korte and Constable, 2011; Nilsson et al., 2014) for Jerusalem. There is an excellent agreement between the different datasets. The data show a steady increase in field intensity from a minimum value at ca. 1800 BCE to a geomagnetic maximum (Iron Age Levantine Anomaly) between the 10th and the 8th centuries with two spikes events. (For interpretation of the references to color in this figure legend, the reader is referred to the web version of this article.)

not including the non-Syrian published datasets shown in Fig. S4, Supplementary material, are problematic correlation between the Mesopotamian, Israeli, and the Egyptian chronologies, and insufficient (or problematic) experimental and chronological information.

Fig. 5 presents a coherent and consistent picture of the geomagnetic field behavior in the first three millennia BCE, where the Mesopotamian and the Israeli datasets show excellent agreement in periods where they overlap, and mutually complement each other where they do not. In the first half of the 3rd millennium BCE the field was relatively low; in the second half of the 3rd millennium BCE the field reached VADM values of up to 110 ZAm^2 and then gradually decreased to a local minimum at ca. 1800 BCE. From ca. 1800 BCE the field intensity increased until the double-peak maximum shown in Fig. 5b, and discussed below. The interpretations shown in Fig. 5 are given in the Supplementary Material.

4.2. A new geomagnetic intensity “spike” in the 8th century BCE

Ben-Yosef et al. (2009) and Shaar et al. (2011) found “geomagnetic spikes” in two radiocarbon dated slag mounds in Southern Israel (Shaar et al., 2011) and Jordan (Ben-Yosef et al., 2009). Spikes

are defined as sub-centennial short-term episodes with extreme high paleointensity values (here defined as exceeding twice the present dipole field value, or $\sim 160 \text{ ZAm}^2$). Two spikes were reported in previous publications: one around 980 BCE, and another around 890 BCE. In addition, Ertepinar et al. (2012) reported very high spike-like values corresponding to a VADM of 177 ZAm^2 in burnt bricks dated to the 11th–10th centuries BCE in Arslantepe, Southern Turkey. Our revised analysis, shown in Fig. 5b shows two samples from the earlier spikes (ca. 980 BCE). The revised field values are slightly different from the ones published in Shaar et al. (2011) owing to the difference in the interpretation process, but still show high fields in excess of 170 ZAm^2 . The published samples with the 890 BCE spike did not pass the stricter criteria we use here suggesting that further research is necessary to establish its reliability. Based on the data shown in Fig. 5 the Arslantepe high field is probably associated with the ca. 980 BCE spike.

One of the most striking results from the new data is a new spike that occurred at the beginning of the 8th century BCE, just before the 732 BCE destruction of Megiddo and Hazor. This spike is seen in the destruction layers Megiddo-H3 and Hazor-V/VI (Fig. 3b) that are dated to Tiglath-Pileser III’s attack on Israel (732 BCE). The

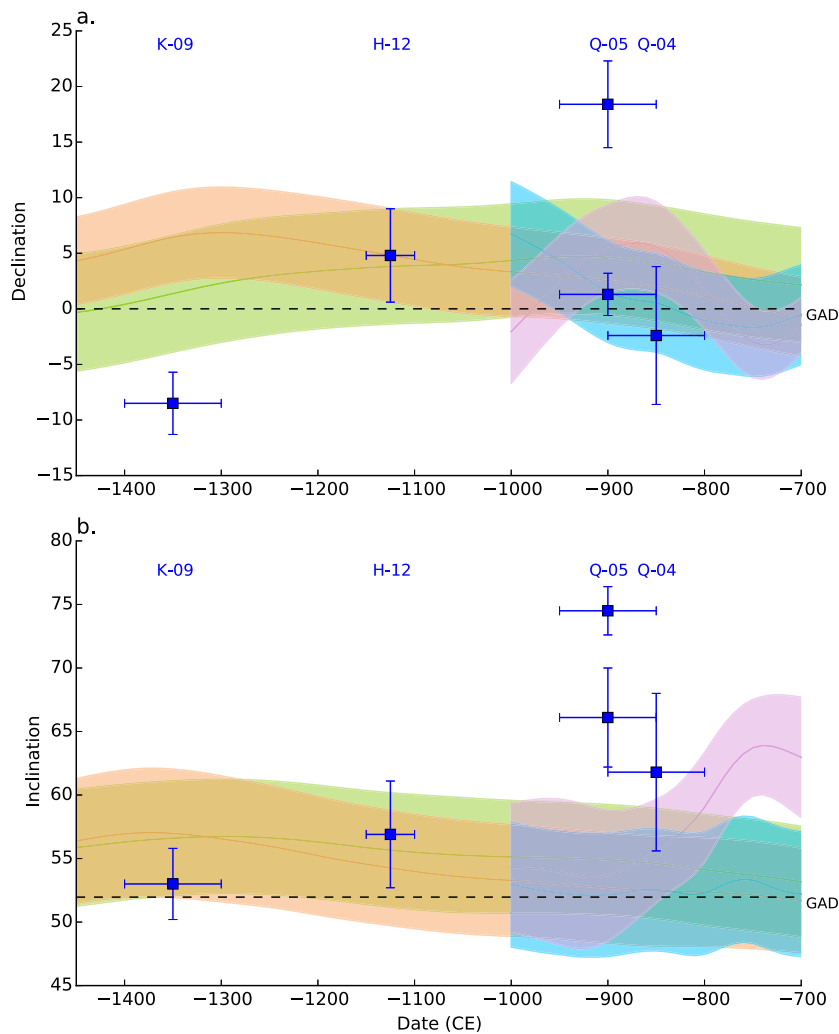


Fig. 6. Paleomagnetic directions from five ovens in Megiddo. (a) Declination, (b) Inclination. Curves show prediction of global geomagnetic models (Korte et al., 2009, 2011; Korte and Constable, 2011; Nilsson et al., 2014) for the location of Megiddo. Geocentric Axial Dipole (GAD) averaged direction is shown as dashed line. The two ovens from the 9th century show deviation from GAD of up to 20° .

samples from these strata were collected from domestic pottery found in the living layers associated with the destruction. Thus, the pottery was manufactured a few decades at the most before the destruction. Owing to the excellent archaeological context, we would expect to obtain a relatively small scatter in the data. Yet, we observe paleointensity data spanning a relatively large interval (75–94 μT in Megiddo and 68–88 μT in Hazor). We interpret this behavior as a new geomagnetic spike event associated with extremely rapid changes in the geomagnetic field. This may be the same feature hinted by the data of Odah (2004) from Egypt in Fig. S4, Supplementary Material.

4.3. Intense local geomagnetic anomaly 10th to 8th century BCE

4.3.1. The Iron Age Levantine anomaly

The paleomagnetic directions in Fig. 6 show high inclination values and substantial deviations of up to 22° (Table 3) from the averaged GAD direction in Tel-Megiddo (declination = 0, inclination = 52.0°) around 900 BCE. This observation suggests that the geomagnetic high field period between the 10th and the 8th centuries BCE is a local anomaly rather than a dipole feature. Figs. 5–6 show in solid curves the prediction of some global geomagnetic models for the Levant area (Korte et al., 2009, 2011; Korte and Constable, 2011; Nilsson et al., 2014). To first order, models based on global compilations predict the general trend

observed in the Levant. Yet, owing to limited coverage and paleomagnetic uncertainties the models underestimate the very high field values seen there.

4.3.2. Comparing the Iron Age Levantine anomaly with SAA

To address the context of the Levantine anomaly we compare the new archaeomagnetic data with the presently active South Atlantic Anomaly (SAA) using the 2015 IGRF geomagnetic field model (Thebaud et al., 2015). Fig. 7a shows the ratio between the total field and the axial dipole component in 2015. Large deviations from axial dipole moment are observed only in the southern hemisphere, in areas affected by the SAA, and they range from 50% to 150%. The Iron Age Levantine anomaly shows a similar pattern (although of an opposite sign): If we assume that the ancient axial dipole moment was less than 100 ZAm^2 (Nilsson et al., 2014) we find that the Levantine spikes exceeded the axial dipole component in factor of about two. Fig. 7b shows the angular deviation of the field vector from the axial dipole field in 2015. Large deviations of more than 20° , such as those observed in the Iron Age Levantine anomaly, occur only near the SAA. Based on these comparisons we infer that the Levantine geomagnetic high was a local geomagnetic feature similar in magnitude to SAA.

In summary, we suggest that the high field episode in the Levant, 11th to the 8th centuries BCE, was a local anomaly similar to the SAA. The Levant Iron Age anomaly is different than SAA in two

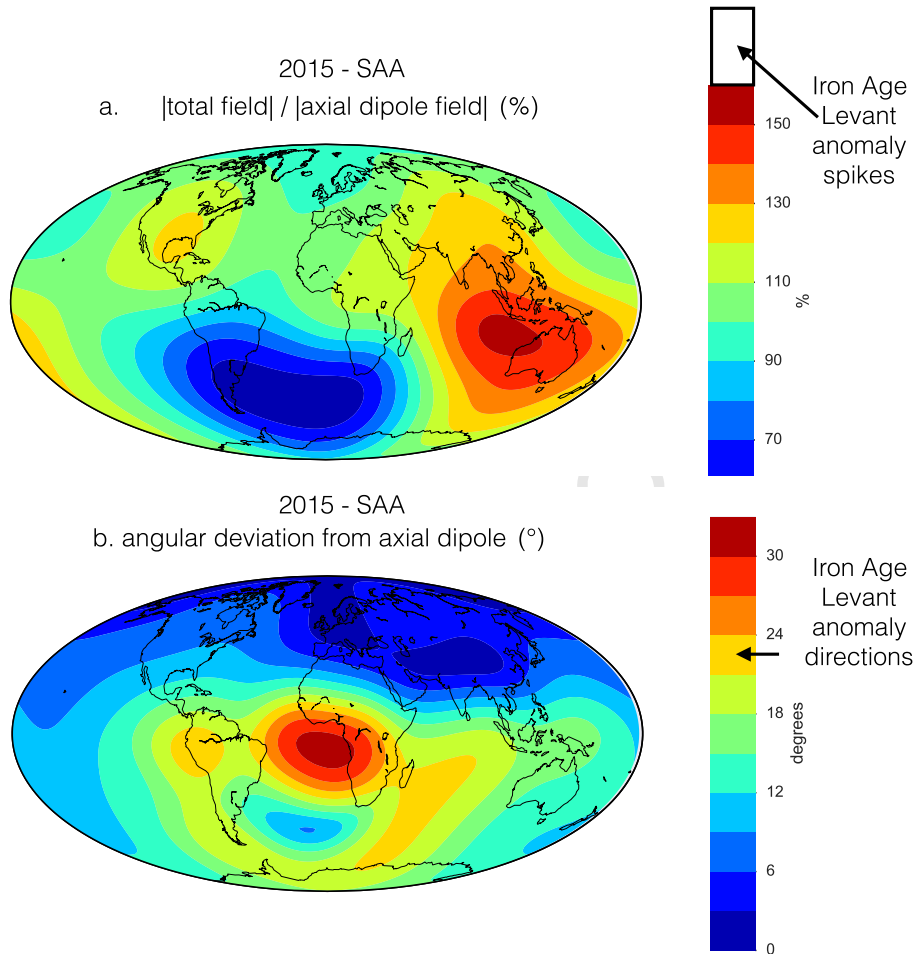


Fig. 7. Geomagnetic field anomalies on Earth surfaces calculated from IGRF12 (Thebaud et al., 2015). (a) Total field versus axial dipole field. (b) Angular deviation from axial dipole field. Large deviations from dipole field are observed only in the southern hemisphere in areas affected by the South Atlantic Anomaly (SAA). The arrows near color bars in the right show the archaeomagnetic values during the Iron Age Levantine anomaly. From this comparison we infer that the Levantine Iron Age anomaly represent a northern hemisphere positive high field anomalies with possibly similar geometry as today's southern hemisphere features. (For interpretation of the references to color in this figure legend, the reader is referred to the web version of this article.)

important aspects: A) the Iron Age Levantine anomaly is a northern hemisphere feature, and B) the Iron Age Levantine anomaly is a positive anomaly. The limits of geographical expression of the anomaly are poorly constrained with the currently available data, however.

5. Summary

We report here 73 new high-precision paleointensity estimates, and 5 new paleomagnetic directions from two key contemporaneous archaeological sites in Israel, Tel Megiddo and Tel-Hazor, covering the period from ca. 3000 BCE to 732 BCE. The new paleointensity data are combined with previously published data from the southern Levant, and analyzed as a whole using an automatic interpretation technique (part of the open code PmagPy software package) and a set of exceptionally strict selection criteria. The new MagIC based compilation of the Levant demonstrates remarkable internal consistency between different sites and source materials (pottery, ovens, slag) and excellent agreement with other data from Syria.

The new data illustrate a steady increase in field intensity from a local minimum at ca. 1800 BCE to a period with exceptionally high field values and fast variations between the 10th and the 8th centuries BCE. This period was accompanied by at least two geomagnetic spikes: one at ca. 980 BCE (Ben-Yosef et al., 2009; Shaar et al., 2011), and another at the beginning of the 8th cen-

tury BCE (new spike reported here). A possibly third, previously published spike, at ca. 890 BCE need further research to establish its reliability.

The Levant Iron Age anomaly is characterized with maximum field values reaching about twice the ancient axial dipole field (following model of Nilsson et al., 2014) and maximal angular deviation from geocentric axial dipole (GAD) of up to 22°. Using the 2015 IGRF model, we see similar deviations from GAD (intensity and direction) only in the southern hemisphere in areas affected by the South Atlantic Anomaly (SAA). This leads us to propose that the Iron Age geomagnetic high in the Levant was a local geomagnetic anomaly similar in scale to SAA, perhaps even larger. Further data are required to establish its geographical extent.

Acknowledgements

We wish to thank Erez Ben-Yosef, Jeff Gee, Cathy Constable, Monika Korte, and Max Brown for very helpful discussions, important suggestions, and constructive comments. We thank Jason Steindorf for helping with the measurements at Scripps Institution of Oceanography. We thank Tel-Megiddo expedition members: Eran Arie, Mario Martin, Norma Franklin, and Yaniv Agmon, for their help in collecting the samples. We thank Lennart de Groot for a thorough review of this manuscript.

Two authors of this article passed away while working on this project after fighting short but courageous battles with cancer. Ha-

gai Ron, a well recognized paleomagnetic pioneer from the Hebrew University of Jerusalem, initiated this project before his early death in September 2012. Sharon Zuckerman, the co-director of the Tel Hazor excavations worked on the archeomagnetic analysis until almost her last days. She passed away in November 2014. We dedicate this article to them. They will be missed.

This project was supported by NSF grant # EAR1345003 to LT, The Israel Science Foundation (grant No. 1181/12 to AA, and grant No. 1364/15 to RS), and Ring Foundation granted to SZ and AA.

Appendix A. Supplementary material

Supplementary material related to this article can be found online at <http://dx.doi.org/10.1016/j.epsl.2016.02.038>.

References

- Ben-Ami, D., 2013. Hazor at the Beginning of the Iron Age. *Near East. Archaeol.* 76, 101–104.
- Ben-Tor, A., 2013. Hazor in the tenth century B.C.E. *Near East. Archaeol.* 76, 105–109.
- Ben-Yosef, E., Ron, H., Tauxe, L., Agnon, A., Genevey, A., Levy, T.E., Avner, U., Najjar, M., 2008a. Application of copper slag in geomagnetic archaeointensity research. *J. Geophys. Res., Solid Earth* 113.
- Ben-Yosef, E., Tauxe, L., Ron, H., Agnon, A., Avner, U., Najjar, M., Levy, T.E., 2008b. A new approach for geomagnetic archaeointensity research: insights on ancient metallurgy in the Southern Levant. *J. Archaeol. Sci.* 35, 2863–2879.
- Ben-Yosef, E., Tauxe, L., Levy, T.E., Shaar, R., Ron, H., Najjar, M., 2009. Geomagnetic intensity spike recorded in high resolution slag deposit in Southern Jordan. *Earth Planet. Sci. Lett.* 287, 529–539.
- Ben-Yosef, E., Tauxe, L., Levy, T.E., 2010. Archaeomagnetic dating of copper smelting site F2 in the Timna valley (Israel) and its implications for the modelling of ancient technological developments. *Archaeometry* 52, 1110–1121.
- Brown, M.C., Donadini, F., Korte, M., Nilsson, A., Korhonen, K., Lodge, A., Lengyel, S.N., Constable, C.G., 2015. GEOMAGIA50.v3: 1. General structure and modifications to the archeological and volcanic database. *Earth Planets Space* 67, 1–31.
- Chauvin, A., Garcia, Y., Lanos, P., Laubenheimer, F., 2000. Paleointensity of the geomagnetic field recovered on archaeomagnetic sites from France. *Phys. Earth Planet. Inter.* 120, 111–136.
- Coe, R., Gromme, S., Mankinen, E., 1978. Geomagnetic paleointensities from radiocarbon-dated lava flows on Hawaii and question of Pacific nondipole low. *J. Geophys. Res.*, 1740–1756.
- Courtillot, V., Gallet, Y., Le Mouél, J.L., Fluteau, F., Genevey, A., 2007. Are there connections between the Earth's magnetic field and climate? *Earth Planet. Sci. Lett.* 253, 328–339.
- de Groot, L.V., Biggin, A.J., Dekkers, M.J., Langereis, C.G., Herrero-Bervera, E., 2013. Rapid regional perturbations to the recent global geomagnetic decay revealed by a new Hawaiian record. *Nat. Commun.* 4.
- de Groot, L.V., Beguin, A., Koster, M.E., van Rijnsing, E.M., Struijk, E.L.M., Biggin, A.J., Hurst, E.A., Langereis, C.G., Dekkers, M.J., 2015. High paleointensities for the Canary Islands constrain the Levant geomagnetic high. *Earth Planet. Sci. Lett.* 419, 154–167.
- Ertepinar, P., Langereis, C.G., Biggin, A.J., Frangipane, M., Matney, T., Okse, T., Engin, A., 2012. Archaeomagnetic study of five mounds from Upper Mesopotamia between 2500 and 700 BCE: further evidence for an extremely strong geomagnetic field ca. 3000 years ago. *Earth Planet. Sci. Lett.* 357, 84–98.
- Finkelstein, I., Piasevsky, E., 2009. Radiocarbon-dated destruction layers: a skeleton for Iron Age chronology in the Levant. *Oxf. J. Archaeol.* 28, 255–274.
- Finkelstein, I., Piasevsky, E., 2010. Radiocarbon dating the Iron Age in the Levant: a Bayesian model for six ceramic phases and six transitions. *Antiquity* 84, 374–385.
- Fisher, R.A., 1953. Dispersion on a sphere. *Proc. R. Soc. Lond.* 217, 295–305.
- Gallet, Y., Butterlin, P., 2015. Archaeological and geomagnetic implications of new archaeomagnetic intensity data from the Early Bronze High Terrace “Massif Rouge” at Mari (Tell Hariri, Syria). *Archaeometry* 57, 263–276.
- Gallet, Y., Genevey, A., Fluteau, F., 2005. Does Earth's magnetic field secular variation control centennial climate change? *Earth Planet. Sci. Lett.* 236, 339–347.
- Gallet, Y., Genevey, A., Le Goff, M., Fluteau, F., Ali Eshraghi, S., 2006. Possible impact of the Earth's magnetic field on the history of ancient civilizations. *Earth Planet. Sci. Lett.* 246, 17–26.
- Gallet, Y., Le Goff, M., Genevey, A., Margueron, J., Matthiae, P., 2008. Geomagnetic field intensity behavior in the Middle East between similar to 3000 BC and similar to 1500 BC. *Geophys. Res. Lett.* 35.
- Gallet, Y., D'Andrea, M., Genevey, A., Pinnock, F., Le Goff, M., Matthiae, P., 2014. Archaeomagnetism at Ebla (Tell Mardikh, Syria). New data on geomagnetic field intensity variations in the Near East during the Bronze Age. *J. Archaeol. Sci.* 42, 295–304.
- Gallet, Y., Montana, M.M., Genevey, A., Garcia, X.C., Thebault, E., Bach, A.G., Le Goff, M., Robert, B., Nachasova, I., 2015. New Late Neolithic (c. 7000–5000 BC) archeointensity data from Syria. Reconstructing 9000 years of archeomagnetic field intensity variations in the Middle East. *Phys. Earth Planet. Inter.* 238, 89–103.
- Genevey, A., Gallet, Y., 2002. Intensity of the geomagnetic field in western Europe over the past 2000 years: new data from ancient French pottery. *J. Geophys. Res., Solid Earth* 107.
- Genevey, A., Gallet, Y., Constable, C.G., Korte, M., Hulot, G., 2008. Archeoint: an upgraded compilation of geomagnetic field intensity data for the past ten millennia and its application to the recovery of the past dipole moment. *Geochim. Geophys. Geosyst.* 9, 23.
- Genevey, A.S., Gallet, Y., Margueron, J.C., 2003. Eight thousand years of geomagnetic field intensity variations in the eastern Mediterranean. *J. Geophys. Res., Solid Earth* 108.
- Halgedahl, S.L., Day, R., Fuller, M., 1980. The effect of cooling rate on the intensity of weak-field TRM in single-domain magnetite. *J. Geophys. Res.* 85, 3690–3698.
- Herve, G., Chauvin, A., Lanos, P., 2013. Geomagnetic field variations in Western Europe from 1500 BC to 200 AD. Part II: new intensity secular variation curve. *Phys. Earth Planet. Inter.* 218, 51–65.
- Hext, G.R., 1963. The estimation of second-order tensors, with related tests and designs. *Biometrika* 50, 353–357.
- Hong, H., Yu, Y., Lee, C.H., Kim, R.H., Park, J., Doh, S.-J., Kim, W., Sung, H., 2013. Globally strong geomagnetic field intensity circa 3000 years ago. *Earth Planet. Sci. Lett.* 383, 142–152.
- Jackson, A., Finlay, C.C., 2007. Geomagnetic secular variation and its applications to the core. In: M. K. (Ed.), *Treatise on Geophysics*. Elsevier, New York, pp. 147–193.
- Jackson, A., Jonkers, A.R.T., Walker, M.R., 2000. Four centuries of geomagnetic secular variation from historical records. *Philos. Trans. R. Soc., Math. Phys. Eng. Sci.* 358, 957–990.
- Jelinek, V., 1978. Statistical processing of anisotropy of magnetic-susceptibility measured on groups of specimens. *Stud. Geophys. Geod.* 22, 50–62.
- Kirschvink, J., 1980. The least-squares line and plane and the analysis of paleomagnetic data. *Geophys. J. R. Astron. Soc.*, 699–718.
- Knudsen, M.F., Riisager, P., 2009. Is there a link between Earth's magnetic field and low-latitude precipitation? *Geology* 37, 71–74.
- Korhonen, K., Donadini, F., Riisager, P., Pesonen, L.J., 2008. GEOMAGIA50: an archeointensity database with PHP and MySQL. *Geochim. Geophys. Geosyst.* 9.
- Korte, M., Constable, C., 2011. Improving geomagnetic field reconstructions for 0–3 ka. *Phys. Earth Planet. Inter.* 188, 247–259.
- Korte, M., Holme, R., 2010. On the persistence of geomagnetic flux lobes in global Holocene field models. *Phys. Earth Planet. Inter.* 182, 179–186.
- Korte, M., Donadini, F., Constable, C., 2009. Geomagnetic field for 0–3 ka: 2. A new series of time-varying global models. *Geochim. Geophys. Geosyst.*
- Korte, M., Constable, C., Donadini, F., Holme, R., 2011. Reconstructing the Holocene geomagnetic field. *Earth Planet. Sci. Lett.* 312, 497–505.
- Kovacheva, M., Boyadziev, Y., Kostadinova-Avramova, M., Jordanova, N., Donadini, F., 2009. Updated archeomagnetic data set of the past 8 millennia from the Sofia laboratory, Bulgaria. *Geochim. Geophys. Geosyst.* 10.
- Kovacheva, M., Kostadinova-Avramova, M., Jordanova, N., Lanos, P., Boyadziev, Y., 2014. Extended and revised archaeomagnetic database and secular variation curves from Bulgaria for the last eight millennia. *Phys. Earth Planet. Inter.* 236, 79–94.
- Lodge, A., Holme, R., 2009. Towards a new approach to archaeomagnetic dating in Europe using geomagnetic field modelling. *Archaeometry* 51, 309–322.
- Nilsson, A., Holme, R., Korte, M., Suttie, N., Hill, M., 2014. Reconstructing Holocene geomagnetic field variation: new methods, models and implications. *Geophys. J. Int.* 198, 229–248.
- Odah, H., 2004. Geomagnetic intensity in Upper Egypt between 2900 BC and 800 AD. *J. Appl. Geophys.* 3, 205–212.
- Paterson, G.A., Tauxe, L., Biggin, A.J., Shaar, R., Jonestrask, L.C., 2014. On improving the selection of Thellier-type paleointensity data. *Geochim. Geophys. Geosyst.* 15, 1180–1192.
- Pavon-Carrasco, F.J., Rodriguez-Gonzalez, J., Luisa Osete, M., Miguel Torta, J., 2011. A Matlab tool for archaeomagnetic dating. *J. Archaeol. Sci.* 38, 408–419.
- Regev, J., Finkelstein, I., Adams, M.J., Boaretto, E., 2014. Wiggled-Matched 14C chronology of Early Bronze Megiddo and the synchronization of Egyptian and Levantine chronologies. *Egypt and the Levant* 24, 241–264.
- Selkin, P.A., Gee, J.S., Tauxe, L., 2007. Nonlinear thermoremanence acquisition and implications for paleointensity data. *Earth Planet. Sci. Lett.* 256, 81–89.
- Shaar, R., Tauxe, L., 2013. Thellier GUI: an integrated tool for analyzing paleointensity data from Thellier-type experiments. *Geochim. Geophys. Geosyst.* 14, 677–692.
- Shaar, R., Ron, H., Tauxe, L., Kessel, R., Agnon, A., Ben-Yosef, E., Feinberg, J.M., 2010. Testing the accuracy of absolute intensity estimates of the ancient geomagnetic field using copper slag material. *Earth Planet. Sci. Lett.* 290, 201–213.

- Shaar, R., Ben-Yosef, E., Ron, H., Tauxe, L., Agnon, A., Kessel, R., 2011. Geomagnetic field intensity: how high can it get? How fast can it change? Constraints from Iron Age copper slag. *Earth Planet. Sci. Lett.* 301, 297–306.
- Shaar, R., Tauxe, L., Gogichaishvili, A., Calvo, R.M., Devidze, M., Licheli, V., 2013. Absolute geomagnetic field intensity in Georgia during the past 6 millennia. *Lat-inmag Lett.*
- Shaar, R., Tauxe, L., Ben-Yosef, E., Kassianidou, V., Lorentzen, B., Feinberg, J.M., Levy, T.E., 2015. Decadal-scale variations in geomagnetic field intensity from ancient Cypriot slag mounds. *Geochim. Geophys. Geosyst.* 16, 195–214.
- Stillinger, M.D., Feinberg, J.M., Frahm, E., 2015. Refining the archaeomagnetic dating curve for the Near East: new intensity data from Bronze Age ceramics at Tell Mozan, Syria. *J. Archaeol. Sci.* 53, 345–355.
- Tauxe, L., 2010. *Essentials of Paleomagnetism*. University of California Press, Berkeley.
- Tauxe, L., Staudigel, H., 2004. Strength of the geomagnetic field in the Cretaceous Normal Superchron: new data from submarine basaltic glass of the Troodos Ophiolite. *Geochim. Geophys. Geosyst.*
- Tema, E., Kondopoulou, D., 2011. Secular variation of the Earth's magnetic field in the Balkan region during the last eight millennia based on archaeomagnetic data. *Geophys. J. Int.* 186, 603–614.
- Tema, E., Gomez-Paccard, M., Kondopoulou, D., Almar, Y., 2012. Intensity of the Earth's magnetic field in Greece during the last five millennia: new data from Greek pottery. *Phys. Earth Planet. Inter.* 202, 14–26.
- Thebaud, E., Finlay, C.C., Beggan, C.D., Alken, P., Aubert, J., Barrois, O., Bertrand, F., Bondar, T., Boness, A., Brocco, L., Canet, E., Chambodut, A., Chulliat, A., Coisson, P., Civet, F., Du, A., Fournier, A., Fratter, I., Gillet, N., Hamilton, B., Hamoudi, M., Hulot, G., Jager, T., Korte, M., Kuang, W., Lalanne, X., Langlais, B., Leger, J.M., Lesur, V., Lowes, F.J., Macmillan, S., Mandea, M., Manoj, C., Maus, S., Olsen, N., Petrov, V., Ridley, V., Rother, M., Sabaka, T.J., Saturnino, D., Schachtschneider, R., Sirol, O., Tangborn, A., Thomson, A., Toffner-Clausen, L., Vigneron, P., Wardinski, I., Zvereva, T., 2015. International Geomagnetic Reference Field: the 12th generation. *Earth Planets Space* 67.
- Toffolo, M.B., Arie, E., Martin, M.A.S., Boaretto, E., Finkelstein, I., 2014. Absolute chronology of Megiddo, Israel, in the Late Bronze and Iron Ages: high-resolution radiocarbon dating. *Radiocarbon* 56, 221–244.
- Wanner, H., Beer, J., Buetikofer, J., Crowley, T.J., Cubasch, U., Flueckiger, J., Goosse, H., Grosjean, M., Joos, F., Kaplan, J.O., Kuettel, M., Mueller, S.A., Prentice, I.C., Solomina, O., Stocker, T.F., Tarasov, P., Wagner, M., Widmann, M., 2008. Mid- to Late Holocene climate change: an overview. *Quat. Sci. Rev.* 27, 1791–1828.
- Zuckerman, S., 2010. "The City, Its Gods Will Return There...": toward an alternative interpretation of Hazor's Acropolis in the Late Bronze Age. *J. Near East. Stud.* 69, 163–178.
- Zuckerman, S., 2013a. Area S: renewed excavations in the Lower City of Hazor. *Near East. Archaeol.* 76, 94–97.
- Zuckerman, S., 2013b. Hazor in the Early Bronze Age. *Near East. Archaeol.* 76, 68–73.

XMLVIEW: extended**Appendix A. Supplementary material**

The following is the Supplementary material related to this article.

Label: MMC 1

caption: ~~Additional supplementary figures and tables referenced in the main text.~~

link: **APPLICATION : mmc1**

Label: MMC 2

caption: Spreadsheets listing the archaeological excavation details of the samples.

link: **APPLICATION : mmc2**

Label: MMC 3

caption: A txt files with paleointensity data of the Levant shown in Fig. 5, main text, produced using the Thellier GUI and the acceptance criteria listed in Table 1.

link: **APPLICATION : mmc3**

Sponsor names

Do not correct this page. Please mark corrections to sponsor names and grant numbers in the main text.

4Q14 NSF, country=United States, grants=EAR1345003

5 Israel Science Foundation, country=Israel, grants=1181/12, 1364/15

UNCORRECTED PROOF



ELSEVIER

Contents lists available at ScienceDirect

Earth and Planetary Science Letters

www.elsevier.com/locate/epsl

Graphical abstract

Large geomagnetic field anomalies revealed in Bronze to Iron Age archeomagnetic data from Tel Megiddo and Tel Hazor, Israel

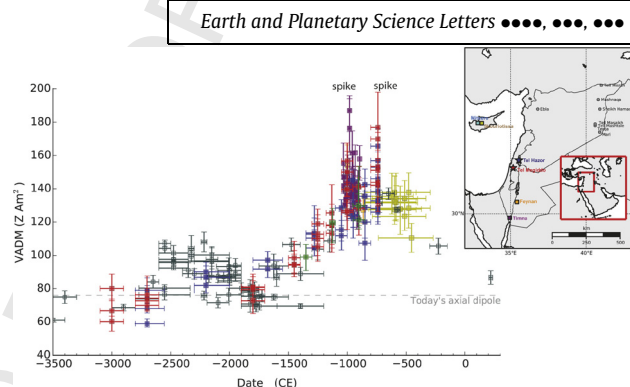
Ron Shaar^{a,b,*}, Lisa Tauxe^b, Hagai Ron^a, Amotz Agnon^a, Yael Ebert^a,
Sharon Zuckerman^c, Israel Finkelstein^d

^a The Institute of Earth Sciences, The Hebrew University of Jerusalem, Jerusalem 91904, Israel

^b Scripps Institution of Oceanography, University of California San Diego, La Jolla, CA 92093-0220, USA

^c The Institute of Archaeology, The Hebrew University of Jerusalem Jerusalem 91905, Israel

^d The Department of Archaeology and Ancient Near Eastern Civilizations, Tel Aviv University, Tel Aviv 6997801, Israel



Highlights

- 73 new archaeointensity estimations and five directional data 3000 BCE to 732 BCE.
- Local geomagnetic anomaly over the Levant from 11th to 8th century BCE.
- A geomagnetic spike found during the 8th century BCE.
- A new archaeointensity compilation of the Levant